



Deposited via The University of York.

White Rose Research Online URL for this paper:

<https://eprints.whiterose.ac.uk/id/eprint/225546/>

Version: Published Version

Article:

Zhang, Hemin, Li, Haojie, Sun, Jiangkun et al. (2025) Coherent Energy Transfer in Coupled Nonlinear Microelectromechanical Resonators. Nature Communications. 3864. ISSN: 2041-1723

<https://doi.org/10.1038/s41467-025-59292-2>

Reuse

This article is distributed under the terms of the Creative Commons Attribution-NonCommercial-NoDerivs (CC BY-NC-ND) licence. This licence only allows you to download this work and share it with others as long as you credit the authors, but you can't change the article in any way or use it commercially. More information and the full terms of the licence here: <https://creativecommons.org/licenses/>

Takedown


If you consider content in White Rose Research Online to be in breach of UK law, please notify us by emailing eprints@whiterose.ac.uk including the URL of the record and the reason for the withdrawal request.

Coherent energy transfer in coupled nonlinear microelectromechanical resonators

Received: 25 April 2024

Accepted: 15 April 2025

Published online: 24 April 2025

 Check for updates

Hemin Zhang^{1,2}✉, Haojie Li¹, Jiangkun Sun², Samuel Kirkbride², Geer Teng¹, Zhenxing Liu¹, Dongyang Chen², Madan Parajuli², Milind Pandit², Guillermo Sobreviela², Chun Zhao³, Weizheng Yuan¹✉, Honglong Chang¹✉ & Ashwin A. Seshia^{2,4}✉

Energy decay, describing the leakage of system energy to the environmental bath, is a universal behavior in oscillators. It has been utilized to elucidate energy transfer between vibrational modes of a resonator. In coupled resonators, achieving an ultra-low coupling rate is essential for observing energy interactions between resonators and environmental bath. Here, we observe periodic transient beating phenomenon by analyzing the transient responses of coupled nonlinear resonators with a coupling rate of 9.6 Hz. The energy transfer rate indicating the hybrid energy manipulation is impacted by asymmetry-induced energy localization and enhanced by nonlinearity. Time-resolved eigenstates, characterized by amplitude ratios, are employed as a quantitative tool to uncover the energy transfer and localization in coupled resonators under nonlinear operations. This work opens the possibilities to manipulate energy transfer, to probe energy localization, and to develop high-precision sensors utilizing the energy transfer between coupled nonlinear resonators.

Coupled microelectromechanical resonators offer valuable model systems for investigating classical and quantum phenomena, mimicking two-level systems and enabling studies of adiabatic passage¹, Landau-Zener transitions², and coherent control^{3–5}. Understanding energy transfer between these coupled resonators is paramount for realizing quantum phononic applications and information processing^{6–8}. For coupled resonators, the vibration energy of a resonator can be coherently transferred to its coupled partner, which means that in addition to dissipating to the surrounding environmental bath, the resonator can also supply energy to or harvest energy from its coupled companion⁹.

However, comprehending such mechanisms remains challenging, particularly in cases involving nonlinearity¹⁰ and structural asymmetry

associated with the coupled resonators. For instance, micro-mechanical resonators are commonly associated with the Duffing nonlinearity. This type of nonlinearity results in an amplitude-frequency (A-f) coupling such that the natural frequency shifts with an increase in vibration amplitude^{11,12} and Saddle-Node bifurcations with transition from the stable branch to unstable branch¹³. Structural asymmetry in coupled resonators induces vibration energy redistribution in the system, also known as the vibration mode localization^{14,15}. Coupled nonlinear modes have been exploited in improved oscillator stability^{16,17} and in the generation of mechanical frequency combs^{18,19} while the vibration mode localization phenomenon has been adapted to provide the basis for an alternative sensing approach^{20,21}. Previous studies on coupled resonators have primarily

¹MOE Key Laboratory of Micro and Nano Systems for Aerospace, School of Mechanical Engineering, Northwestern Polytechnical University, Xi'an, China.

²Department of Engineering, The Nanoscience Centre, University of Cambridge, Cambridge, UK. ³School of Physics, Engineering, and Technology, University of York, York, UK. ⁴Department of Electrical Engineering, Indian Institute of Technology Bombay, Powai, Mumbai, India. ✉e-mail: zhanghm@nwpu.edu.cn; yuanwz@nwpu.edu.cn; changhl@nwpu.edu.cn; aas41@cam.ac.uk

featured typical coupling rates spanning from GHz²², MHz⁴ to kHz levels²³. Consequently, the coherent energy transfer represented by the beating patterns is not directly visible as the energy transferred every cycle is too low to be recognized, if the coupling rate is too high. The energy transfer between modes of a single resonator structure has been studied with the utilization of necessary tools including parametric pump^{23–26} and internal resonance^{27–29} to generate lower coupling rates. Both parametric pump and internal resonance methods are fundamentally limited by coherence loss when parameters deviate, or internal resonance is disrupted. Direct mechanical coupling between resonators with a low coupling rate is an evident choice for observing energy transfer. However, at low coupling rates, the coupled resonators become highly sensitive to even slight perturbations. There is a significant gap in studies investigating the complex dynamics of energy transfer in such systems, particularly when considering the role of nonlinearity in this modulation.

This paper introduces a mechanically coupled resonator system with an ultra-low coupling rate of 9.6 Hz, allowing for the direct observation of energy exchange between resonators through the measured transient response. The transient energy balance analysis reveals that nonlinearity plays a crucial role in amplifying the energy transfer rate. Furthermore, this study demonstrates that the transient amplitude ratio can quantitatively capture the intrinsic energy transfer and localization phenomena that are not accessible through conventional frequency sweep-based measurement approaches. This work provides valuable insights and framework into the complex dynamic energy transfer behaviors in microelectromechanical coupled nonlinear resonators, potentially opening the avenues for the fields of sensing, energy harvesting, and signal processing.

Results

Design and characterization of the coupled resonators

The proposed coupled micromechanical resonators system (Fig. 1a) was constructed with two double-ended-tuning-fork (DETF) resonators connected via a mechanical disc coupler anchored at the base³⁰. The mechanical coupling between resonators is facilitated by the slight deformation of the coupler, due to the stress generated when the two tines of a resonator vibrate in parallel. The coupling is geometry dependent and can be manipulated by designing the parameters of the coupler, as detailed in Supplementary Information Note 1. The resonators are capacitively actuated and sensed via the electrodes on either side of the tines. The device is excited only by thermal noise, when the two switches are off. We therefore obtain the intrinsic natural frequencies of the first two modes: $\omega_1/2\pi \approx 122721.6\text{Hz}$ and $\omega_2/2\pi \approx 122731.2\text{Hz}$, as shown in Fig. 1c. Such a state of two modes having equivalent amplitudes is named as the symmetric state, at where the frequency split $\Delta\omega/2\pi \approx 9.6\text{Hz}$ between the two modes is lowest. This split is referred to as the coupling rate ($\Delta = 9.6\text{Hz}$), as it is proportional to the coupling factor of the system, which is defined by the ratio between coupling stiffness (k_c) and stiffness of the resonator (k). The coupling factor can be experimentally characterized by using the coupling rate^{15,31} $\kappa = \Delta\omega/\omega_1 \approx 7.82 \times 10^{-5}$.

The other critical parameter of the coupled resonators is the quality factor (Q), which demonstrates the energy dissipation of resonators to the environmental bath. For our device, $Q \sim 42000$ is characterized by using the -3dB bandwidth method³² for resonators at both modes, demonstrating a damping rate of $\gamma \approx 1.46\text{Hz}$. This calculated damping is applicable in linear operating conditions without modal overlap. Our subsequent theoretical and experimental studies will explore how damping behaves under conditions of significant energy exchange with structural asymmetry and Duffing nonlinearity. Based on the comparisons of $\kappa > 1/Q$ and $\Delta > \gamma$, and the case that there is no modal overlap between modes in the linear regime, the coupled resonators system is considered to be operating in the strong coupling

regime^{33–35} with resonators exchanging energy more rapidly than dissipating to the environmental bath.

The experimentally measured noise spectra of the two resonators demonstrates a base voltage noise level of $\sim 300\text{ nV}/\sqrt{\text{Hz}}$. With the variation of the tuning voltage, avoided crossing¹³ and loci veering is observed as shown in Fig. 1d, e, splitting this diagram into an upper branch as the representative of the higher-frequency mode (ω_2) and a lower branch as the representative of the lower-frequency mode (ω_1). The energy gets redistributed and confined to a particular mode with δ deviating from the symmetric point where $V_{\text{Tuning}} = -5.85\text{ V}$. The measurements align remarkably well with the theoretical analysis in Supplementary Information Note 2 and Fig. S4. Combining energy redistribution and loci veering, it can be remarked that mode localization^{36,37} is evident as an intrinsic character of the coupled resonators. This experimental observation of thermal noise spectra offers an alternative visualization of localization, contrasting with the frequency sweeping method as shown in Supplementary Information Fig. S5.

Frequency responses analysis with nonlinearity

When concerning the coupling, cubic nonlinearity term and noise and assuming the resonators have equivalent damping, the dynamic equations of the system can be written as:

$$\ddot{x}_1 + \dot{x}_1\omega_0/Q + \omega_0^2(1 + \kappa + \beta_1 x_1^2)x_1 - \kappa\omega_0^2 x_2 = (f + \xi_1(t))/m \quad (1)$$

$$\ddot{x}_2 + \dot{x}_2\omega_0/Q + \omega_0^2(1 + \kappa + \delta + \beta_2 x_2^2)x_2 - \kappa\omega_0^2 x_1 = \xi_2(t)/m \quad (2)$$

where x_1 and x_2 are the displacements of the coupled resonators, ω_0 the initial natural frequency, $\delta = \Delta k/k$ the stiffness asymmetry between resonators, k the symmetric resonator stiffness, $\omega_0 = \sqrt{k/m}$ the initial frequency of the first mode, $f = F \sin(\omega t + \theta)$ the applied force to Res 1, and $\xi_1(t)$ and $\xi_2(t)$ the random noisy forces. Nonlinear springs for the two resonators are defined as $k_{n1} = k(1 + \beta_1 x_1^2)$, and $k_{n2} = k(1 + \beta_2 x_2^2)$, where β_1 and β_2 are the Duffing nonlinear coefficients.

With drive level rising, nonlinear response is evident characterized by an increased in the natural frequency with drive level, which is defined as stiffness hardening effect or amplitude-frequency (A-f) effect, as shown in Fig. 2. The linear and nonlinear frequency responses can be theoretically modelled based on Eqs. (1) and (2) using the multiple scales method³⁸. In the nonlinear regime, the coupled resonators demonstrated Saddle-Node bifurcations¹³ with transition from the stable branch to the unstable branch for both modes, as shown in the upper plots in Fig. 2, and Supplementary Information Fig. S10.

In the symmetric scenario with $\delta \approx 0$, the coupled resonators exhibit similar stiffness hardening effect, implying comparable A-f curvatures, with equivalent nonlinear coefficients for both modes: $\beta_1 = \beta_2 \sim 1.0 \times 10^{10}\text{ m}^{-2}$. The onset of nonlinearity marking by the critical amplitudes³⁹ is evaluated by numerical simulation, as shown in Fig. S9. The nonlinear terms here are extracted using the fitting equation³⁹ $\omega = \omega_0(1 + \frac{3}{8}x^2\beta)$, while the backbone curves of the coupled resonators demonstrating the A-f effect are numerically modelled using the derivations (S24a) and (S24b) in Supplementary Information Note 3.

In the asymmetric scenario, vibrational energy is redistributed due to mode localization³⁷. In such a case, the vibration amplitude and frequency coupling behaviors are further modified. The apparent A-f effect is modulated simultaneously by nonlinearity and degree of asymmetry. The nonlinear coefficients of the two resonators at the two modes can no longer be fitted well using the above fitting equation³⁹, but should be fitted using the derivations from Supplementary Information equations (S24a, b). This can be explained by the presence of the apparent amplitude-dependent damping effect in asymmetric cases. While our theoretical framework explicitly assumes the absence

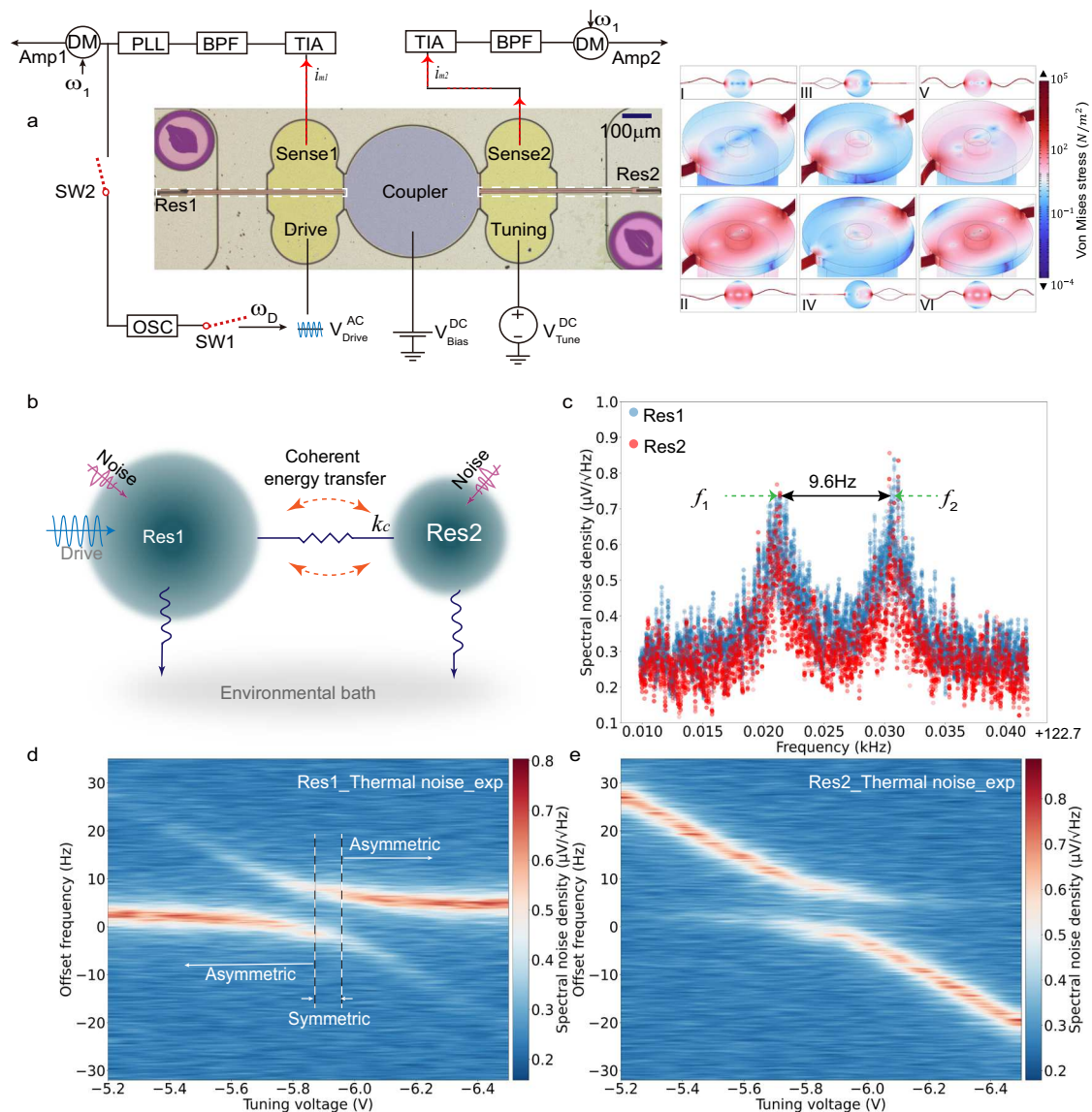


Fig. 1 | Illustration of the coupled resonators and experimentally measured noise spectral density. **a** False-color optical image of the coupled resonators and associated electrical measurement interface. The finite element simulations on the right indicate how the two resonators are coupled together. The modes I, II, V and VI where the two tines vibrate in parallel are of particular interest while the modes III and IV where the two tines vibrate in the opposite direction are not because there is almost no coupling at these modes. Dimensions of the device are provided in Supplementary Information Table SII. TIA here indicates transimpedance amplifier, BPF the bandpass filter, PLL the phase-locked-loop module including a phase delay, DM the demodulator, OSC the digital oscillator, Amp the amplitude of a specific resonator, and SW the control switch. PLL, DM, OSC and amplitude recording are all

realized by the integrated components in Zurich Instruments HF2LI lock-in amplifier. **b** Model of the coupled resonators, showing the noise, drive and dissipation. The environmental bath here indicates all dissipation means of a resonator including the air damping, anchor damping, and thermoelastic damping. **c** Measured thermal noise of the two resonators in case there is no structural mismatch between resonators. **d, e** Measured spectral density of the thermal noise of Res 1 (**d**) and Res 2 (**e**) with different tuning voltages (from -6.5 V to -5.2 V with a step of 0.05 V) when switches were cutoff. The simulated data can be found in Supplementary Materials Fig. S2. The DC bias voltage was set as 10 V in all experiments. Source data are provided as a Source Data file.

of nonlinear damping terms in the governing equations, the asymmetric coupled resonator system exhibits apparent amplitude-dependent damping characteristics, as shown in Supplementary Fig. S11c, d. These are observable through comparative analysis of force-normalized response amplitudes under conditions of stiffness mismatch. Such apparent nonlinear responses set limitations in observing energy transfer and localization using conventional frequency-domain analysis due to the absence of discernible mode splitting or intermodal energy transfer in frequency-swept responses in nonlinear operation cases as shown in Fig. S12. This characterization necessitates time-resolved transient analysis of ringdown dynamics, where energy transfer can be observed through decay rate extraction.

Nonlinear characterization with transient responses

The amplitude decay of a single resonator is the transient response when switching off the actuation. It is of an exponential nature with the decay time related to the damping rate $\gamma = m\omega/Q$ ^{40,41}. Energy decay in coupled resonators is more complicated as it may show significant beating²⁹ or Rabi oscillations^{41–43}. However, the beating phenomenon is not always observable in coupled resonators in previous studies, as it requires a sufficient low coupling rate to facilitate noticeable energy transfer. Our basic coupling rate of $\Delta = 9.6$ Hz provides sufficient energy transfer per cycle, and our ringdown phase-locked-loop measurement setup ensures the possibility of tracking the evolution of the transient responses.

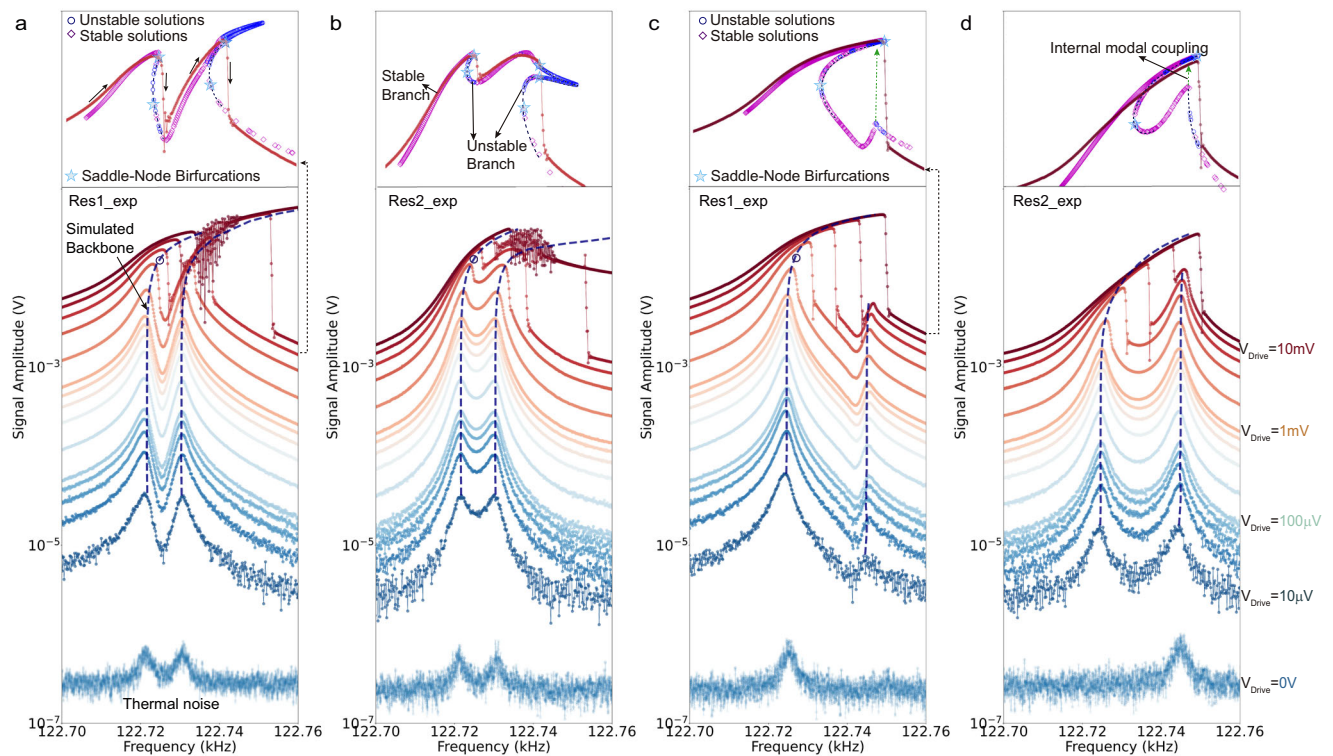


Fig. 2 | Transmission spectra of the coupled resonators with the theoretical analysis on the backbone curves and stable analysis. **a, b** Responses of the two resonators with different drive AC levels when the system is approximately symmetric ($V_{\text{Tuning}} = -5.85$ V). **c, d** Responses with different drive AC level when the system is asymmetric ($V_{\text{Tuning}} = -5.2$ V). The sweeping method here is forward sweeping as indicated by the solid black arrows in the upper plot in (a). The backbone curve, i.e., the amplitude-frequency (A-f) effect showing the shift in frequency with increasing amplitude is observable for the resonators in both the symmetric and asymmetric cases. The dashed backbone curves in (a–d) are drawing using simulated data based on the extracted peak amplitudes in the experiments and the theoretical equations in Supplementary Information equations (S24a, b). The fitting nonlinear coefficients for both modes and both resonators in symmetric cases are $\beta_1 \sim \beta_2 \sim 1.0 \times 10^{10} m^{-2}$. In asymmetric cases, the fitting nonlinear coefficients for Res 1 are $\beta_{11} = 2.2 \times 10^{10} m^{-2}$ for the 1st mode, $\beta_{21} = 7.5 \times 10^{10} m^{-2}$ for the

2nd mode, and for Res 2 are $\beta_{21} = 7.4 \times 10^{10} m^{-2}$ for the 1st mode, $\beta_{22} = 2.0 \times 10^{10} m^{-2}$ for the 2nd mode which are affected by the apparent nonlinear damping effect. It can be found that the effective nonlinear A-f effect is significantly modulated by the extent of energy localization. The theoretically analyzed and experimentally measured frequency responses of the coupled resonators with a specific drive AC of 8 mV are shown at the top of the figure corresponding to different configurations. The navy circle indicates the unstable solutions while the magenta diamonds represent the stable solutions. Only stable points can be extracted in the frequency sweep. There are critical amplitudes that the resonators operate from the linear regime transitioning to the nonlinear regime³⁹. Bifurcations are clearly seen while transitioning to the Duffing-dominated nonlinear regime. The green dashed arrows in the top insets of c and d indicate the intermodal coupling of the system. Source data are provided as a Source Data file.

The time-resolved transient signal amplitudes of the two resonators with initial drive AC of 5 mV and 20 mV are shown in Fig. 3a, b. A significant beating phenomenon can be observed. The first pulse is with energy being transferred from Res 1 to Res 2 and exactly in the moment when all energy is transferred, the amplitude of Res 1 keeps constant, and Res 2 starts to transfer energy back. Both spectrogram and PLL-tracking results demonstrate frequency coinciding with the natural frequency of the coupled system i.e., $\omega_1/2\pi$. If the two resonators operate nonlinearly, the spectrogram in Fig. 3d shows a progressive decreasing frequency from -122.740 kHz which is the result of the A-f effect, and ultimately converges to the corresponding small-amplitude eigenfrequency $\omega_{1, \text{linear}} \sim 122.727$ kHz which is defined by the structural asymmetry δ . More frequency and amplitude ringdown information can be found in Supplementary Information Fig. S18.

The phase difference between resonators, as depicted in Fig. 3e, f, demonstrates a locked condition with excitation on, yielding a mean value $\Phi_0 \sim -0.25$ radians, in good agreement with our measurements using the frequency-phase sweep method (Fig. S8). When ringdown starts, the phase difference shows oscillatory variations between $\Phi_{\text{max}} \sim 0.38$ radians and Φ_{min} close to Φ_0 . It

is known that the in-phase mode and out-of-phase mode introduce a phase difference of $\Phi = 0$ and $\Phi = \pi$, respectively. Such oscillatory observations on phase difference indicate that the resonators are oscillating close to the in-phase mode in the steady state and vibrate in a hybrid mode resulting from the superposition of both modes during the ringdown process.

By extracting the envelopes of transient signals, the amplitude ringdown curves can be obtained. As the frequency of Res 1 has been tracked using a PLL, it is easy to draw the amplitude-frequency plot in the ringdown process, as indicated in Fig. 3g–j. It is interesting that the resonator initially vibrates nonlinearly, followed by an amplitude and frequency decrease aligning the A-f curves as that in the frequency sweeping section in Fig. 2a, c until converging to its intrinsic low-amplitude frequency, which is also verified in Fig. S18. The ringdown trajectory of Res 1 always follows the nonlinear backbone curves exactly, which can be fitted using the fitting equation³⁹ $\omega = \omega_0(1 + \frac{3}{8}x^2\beta)$, as shown in Fig. Fig. S16. However, for Res 2, the ringdown trajectories do not follow such fitting equation if the coupled resonators are asymmetrically localized, as indicated by Supplementary Information Fig. S17, which is attributed to the apparent amplitude-damping in the asymmetrically coupled resonators.

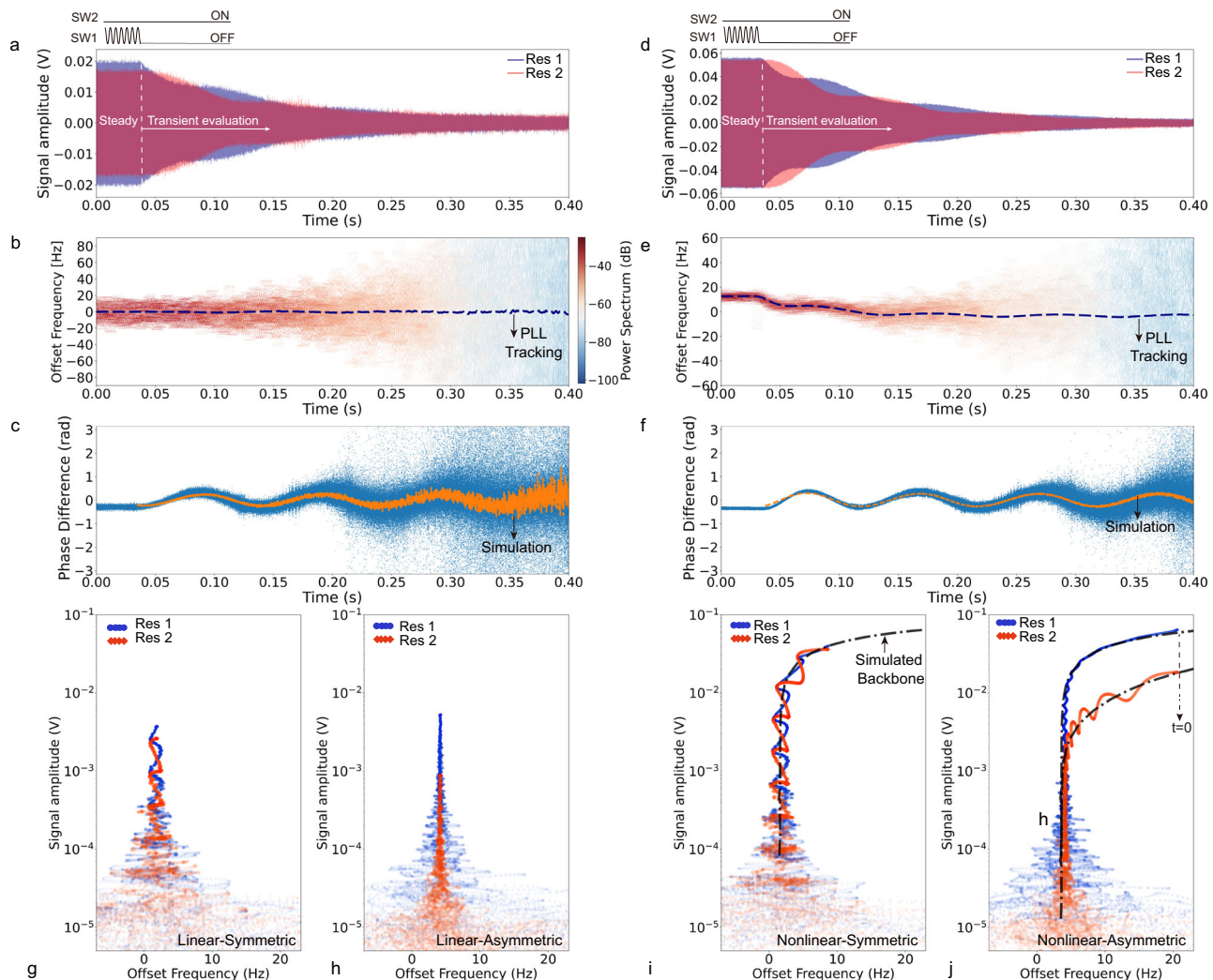


Fig. 3 | Comparison of the transient responses of the coupled resonators.

Steady and transient responses of the coupled resonators when the drive AC level is 5 mV (a) and 20 mV (d). The corresponding frequency-time spectrograms of Res 1 with linear color (b) and nonlinear steady configurations (e), respectively. b, e share the same color bar. The dashed-line frequencies are collected using the Phase-Locked-Loop (PLL) tracking mechanism as introduced in Method. The resonant frequency of Res 1 when working in the nonlinear regime exhibits oscillatory decline, eventually converging to an intrinsic value dictated by structural asymmetry. In the experiments, switch SW2 is always on to track the frequency and demodulate the signal, whereas switch SW1 is cut off at a specified time and to commence

measurement of the ringdown responses. The corresponding phase differences between resonators are extracted in (c, f). The orange lines indicate the theoretically analyzed phase differences using equation (S23) in Supplementary Information. Reproduction of the A-f effects with linear symmetric case (g), linear asymmetric case (h), nonlinear symmetric case (i) and nonlinear-asymmetric case (j). The frequencies used in (g–j) are collected using the PLL tracking method. The offset frequency here is the subtraction results of the measured frequency with the reference frequency of 122.727 kHz. The marker ‘t = 0’ in (j) indicates the start of the ringdown. Source data are provided as a Source Data file.

Energy transfer with Duffing nonlinearity

Another key result is related to the capacity to manipulate energy transfer by adjusting the initial conditions of the coupled resonators, such as asymmetry and nonlinearity. For this purpose, we changed the initial conditions and recorded a series of ringdown responses for an energy balance analysis. When Res 1 was initially actuated linearly with a drive AC of 1 mV while Res 2 was perturbed by δ , clear beating phenomenon can be observed in ringdown curves as shown in Fig. 4a, b. The simulations in Supplementary Information Fig. S13 closely aligns with the experimental results.

The total energy E_{Total} contains the potential energy of each resonator proportional to the summation of the linear and nonlinear square displacement $\frac{1}{2}k_i x_i^2 + \frac{1}{4}\beta_i x_i^4$ and the coupling energy $E_{coupling} = \frac{1}{2}k_c(x_1 - x_2)^2$ stored in the coupler, as analyzed in the Supplementary Information Note 5. E_{Total} is always decaying exponentially no matter with or without nonlinearity and asymmetry, revealing a constant damping rate of $\gamma_0 = 1.51\text{Hz}$, as shown in Fig. 4i. This damping

to the environmental bath includes all the dissipation like anchor damping, thermo-elastic damping and air damping⁴⁰. This γ_0 is equivalent to that of the coupled resonators with deep asymmetry ($V_{\text{Tuning}} = -4.5\text{V}$) as shown in Fig. 4a, which is extracted based on the fitting equation of $x_1 = \chi e^{-2\gamma_0 t}$ and the method of recording the serial damping rates are introduced in Supplementary Information Note 5 and Fig. S20. The value of γ_0 also matches with the calculation of $Q = \omega_0 / 4\pi\gamma_0$ using the -3dB bandwidth measurements in the frequency response section.

The alternating energy exchange pattern of the resonators in suggest timely-variable damping rates. Such variable damping rates are evidence of energy transfer as the exchanged energy offsets the dissipation of Res 1 and Res 2. To quantitatively describe the energy transfer between resonators, the time-variable energy decay rates γ_i ($i = 1, 2$) of each resonator are extracted using the slice-fitting method shown in Supplementary Information Note 5. We define the energy transfer rate as $\zeta_i = \gamma_i - \gamma_0$. The case of $\zeta_i = 0$ means that the energy of

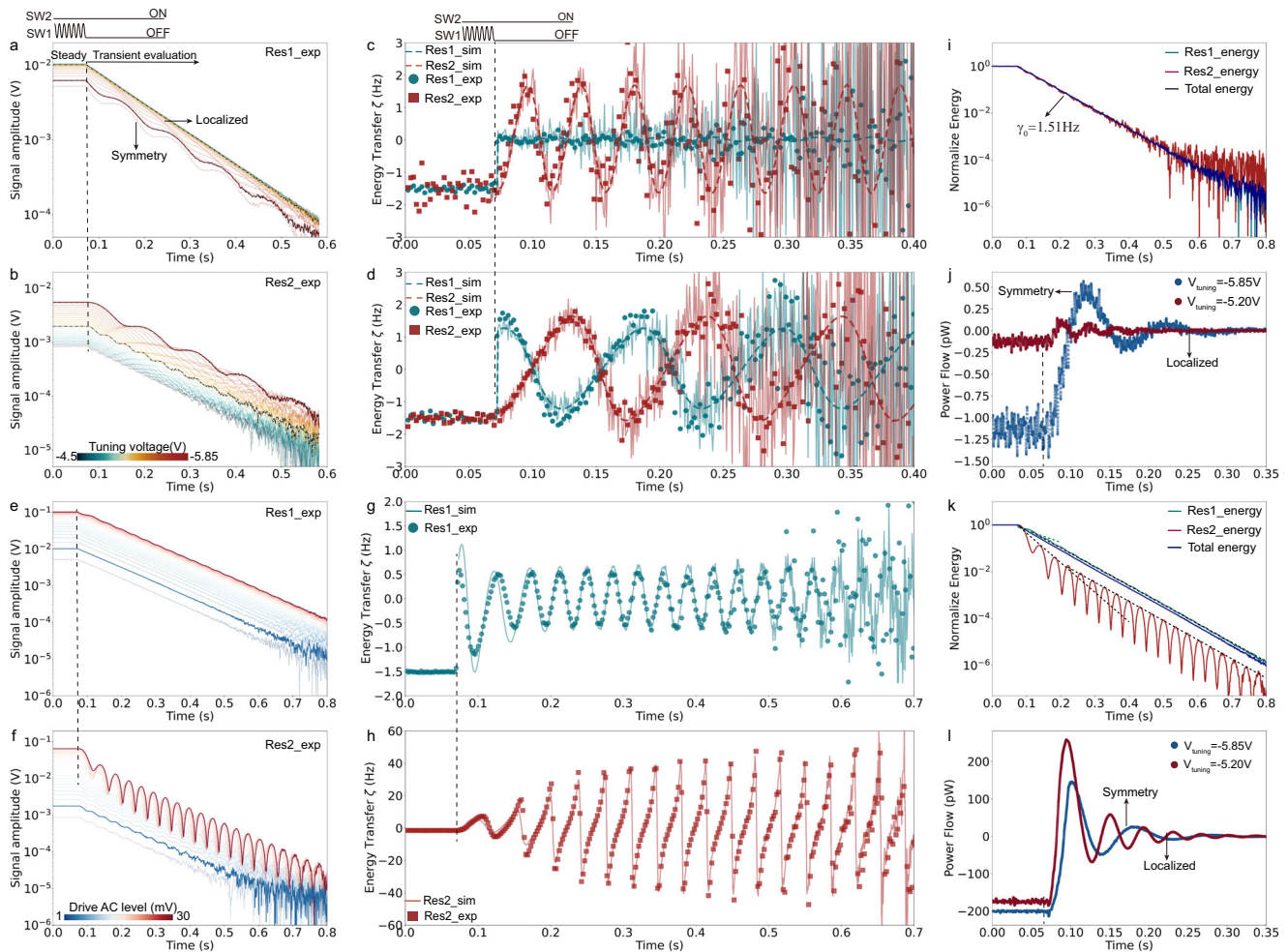


Fig. 4 | Ringdown characterization of the coupled resonators under the influence of asymmetry and nonlinearity. **a, b** Transient evaluation of Res 1 (**a**) and Res 2 (**b**) demodulated by ω_1 as a function of the tuning voltage from -4.5 V to -5.85 V with a step of 0.05 V. **c** Experimentally recorded and theoretically simulated energy transfer rates of resonators at the asymmetric point (**c**) with a tuning voltage of -5.2 V, and at the symmetric point (**d**) with a tuning voltage of -5.2 V 5.85 V. Detailed calculation method of the energy transfer rate can be found in Supplementary Information Note 5. The dashed curves in (**c**, **d**) are the simulation results without random noise while the solid curves are simulated results with random noise. **e, f** Transient responses of Res 1 and Res 2 demodulated by ω_1 with different drive AC levels from 1 mV to 30 mV with a tuning voltage of -5.2 V. In the steady state, the resonators are locked at the 1^{st} mode in linear cases and mild nonlinear cases without modal interaction and at the top bifurcation when the two modes are

interacted together. **g, h** Experimentally measured, and theoretically simulated decay rates of Res 1 and Res 2 are based on the data with a drive level of 30 mV in (**e**, **f**). The method of calculating energy transfer rates can be found in Supplementary Material Note 4. **i, k** Normalized energy of the two resonators as well as the system total energy, with a drive level of 1 mV (**i**) and 30 mV (**k**), respectively. The total energy decrease indicates a decay rate of $\gamma_0 = 1.51$ Hz which is the average damping rates for both Res 1 and Res 2 in (**i**). The difference in the slope indicates the transition of the resonator from the nonlinear to the linear operation regime. **j, l** Power flow between resonators in the linear (**j**) and nonlinear (**l**) initial configurations, calculated using the corresponding navy and red data in (**e**, **f**) in conjunction with the equations provided in Supplementary Information equation (S41). Source data are provided as a Source Data file.

the mode is only dissipated to the environmental bath, and there is almost no internal exchange between resonators. The case of $\zeta_i > 0$ means that this specific resonator is releasing more energy to its coupled companion than to the environmental bath. Vice versa, $\zeta_i < 0$ means that the resonator is scavenging from its coupled companion more than dissipation to the environment bath. The specific case of $\zeta_i = -1.5$ Hz is the initial steady state with external energy compensating the dissipation to the environment.

As expected, it is Res 1, the directly actuated resonator, that first exhibits the abrupt energy loss, transiting from $\zeta_1 \approx -1.5$ Hz to $\zeta_1 \approx 1.5$ Hz. The oscillation rate at which the energy transfer occurs varies with δ , as shown in Supplementary Information Fig. S21. With linear initial states, the statistic maximum and minimum values of ζ are $\sim \gamma_0$ and $\sim -\gamma_0$, suggesting that the energy exchanged between resonators is at most twice the energy dissipated due to damping. The periodic oscillation of ζ in Fig. 4c, d are attributed to the energy

coupling and transfer between resonators. There is no apparent amplitude-dependent damping in this case as shown by the energy ringdown curves in Fig. 4i where the mean slopes are similar for Res 1, Res 2 and the total energy during the whole process.

A significant difference with nonlinear initial states is that the maximum value of ζ for Res 2 is much larger than γ_0 , as high as >40 Hz as shown in Fig. 4h. This implies that the scavenged and lost energy of Res 2 can significantly surpass its intrinsic energy dissipation. The average damping rate of Res 2 in the deep nonlinear configurations is higher than γ_0 as shown in Fig. 4h, and the average of Res 1 is lower than γ_0 correspondingly. The coupling rate in the nonlinear regime varies with time and finally converges to its intrinsic value defined by the asymmetry δ if the resonators are initially vibrating nonlinearly, as indicated by Supplementary Information Fig. S21b.

The ringdown responses of the asymmetrically ($V_{\text{Tuning}} = -5.20$ V) coupled resonators with increasing drive AC are shown in Fig. 4e, f,

while the corresponding simulations are provided in Supplementary Information Fig. S12. A key observation is that the amplitudes of the resonators have more visually apparent oscillatory behavior in the nonlinear regime, indicating the enhancement of energy exchange. This enhancement can be quantitatively assessed by examining the power flow²⁷, as illustrated in Fig. 4j, l. It is obvious that with linear initial configuration, the highest power flow will significantly decrease by a factor of 4, when the tuning voltage changes from $V_{\text{Tuning}} = -5.85$ V (the symmetric case) to $V_{\text{Tuning}} = -5.20$ V (the localized case). On the contrary, if the initial configuration is nonlinear with a drive AC of 26 mV, the highest power flow in the localized case increases by a factor of 2. The maximum power flow during the ringdown process as a function of Drive AC level and perturbation voltage is shown in Supplementary Information Fig. S22, clearly demonstrating the comprehensive manipulation of nonlinearity and localization on energy transfer.

With the impact of the apparent amplitude-dependent damping induced by the asymmetry, the damping rates decrease to a specific converged value for Res 1 whereas that of Res 2 increases from the start of the ringdown, as shown in Fig. 4g, h. Apparent amplitude-dependent damping is also observable in Fig. 4k where the initial decaying of Res 1 is slower while Res 2 is faster. The effective damping rates of the two resonators depend on the amplitude ratios X_1/X_2 as well as the phase difference, which will be modulated by structural asymmetry and nonlinearity as explained in Supplementary Information Note 3.

Furthermore, if we continue increasing the actuation level to >100 mV, 1:1 internal resonance with frequency locking is seen, as shown in Supplementary Information Fig. S6. In this state, both frequency and amplitude are locked^{27,28}, as shown in Fig. S7. The ringdown responses with such initial frequency locking are demonstrated in Fig. S23. There is a period where the energy of the two resonators is released at a constant rate of ~40 Hz no matter the level of initial asymmetry. This period is named as the internal resonance release regime.

Energy localization in coupled nonlinear resonators

Previous experiments in Fig. S12 have demonstrated that the energy localization behaviours in the asymmetrically coupled nonlinear resonators cannot be revealed clearly using the frequency-domain analysis even though previous research has demonstrated mass sensors operating in this regime⁴⁴. The eigenstate, represented by the amplitude ratio X_1/X_2 , is the other intrinsic metric of the coupled resonators¹⁴. Therefore, its transient dynamic processes would provide additional insight into system dynamics and intrinsic nature. The time-domain transient amplitude ratio measurements provide us with the possibility of revealing further insights into the behavior in this regime, both qualitatively and quantitatively.

It can be seen from Fig. 5a that the time evolution of the amplitude ratio has similar oscillatory characters as that of the energy transfer rates in Fig. 4a, b. We integrated all the amplitude ratio ringdown responses of the coupled resonators with linear initial states and positive and negative perturbations ranging from $V_{\text{Tuning}} = -4.00$ V to $V_{\text{Tuning}} = -7.60$ V in Fig. 5b, c. This is another kind of portrait of the energy localization phenomenon shown in Fig. 1d, e.

If the initial operation state is nonlinear, the heightened asymmetry amplifies the oscillatory frequency as well as the energy transfer as shown in Fig. 5e, f. At the same time, only one mode, here the 1st mode can be identified as the device demonstrates considerable stiffness hardening. Notably, the time-domain amplitude ratio evolution method can still reveal the energy localization in Duffing nonlinear or even 1:1 internal resonance regime as provided in Fig. S23, which is a significant advantage over the swept frequency response method. For both linear and nonlinear configurations, the coherence time decreases as structural asymmetry and noise increase. Introducing larger perturbations in the coupled resonators results in shorter lifetimes and

noisier amplitude ratios during the ringdown process. The linear configurations exhibit a more pronounced sensitivity to perturbations, leading to accelerated decoherence, whereas the nonlinear configuration demonstrates greater robustness against such disturbances. This is in good match with our previous prediction that the best resolution using amplitude ratio as sensor output metric is around the symmetric line³⁷. As demonstrated previously, the apparent amplitude-dependent damping emerges simultaneously with the mode localization effect, as they both present only in cases when resonators are asymmetrically coupled. Such coexistence results in complicated quantitative determination through systematic analysis of the coupling-governed phase term $\sin(\Phi)$ under parameter variations as indicated in Supplementary Information Note 3.

Discussion

The decay investigation of coupled nonlinear resonators holds significant promise for advancing our understanding of two-level systems and enabling the development of high-precision sensors. Distinguishing from the observations of energy transfer using with the aid of parametric pump^{23,24} or internal resonance⁴⁵, here in this paper, using a mechanically coupled resonators system with an ultra-low coupling rate ~9.6 Hz, we directly observed the amplitude decay process illustrating oscillatory energy exchange with the beating phenomenon, in both linear and nonlinear configurations. The ringdown processes initiated with nonlinear operation configurations can accurately replicate the A-f effect^{10,46}. However, the damping of the coupled resonators is revealed to be modulated by the structural asymmetry induced energy localization, demonstrating apparent amplitude-dependent damping in the asymmetrically coupled resonators. This leads to distinct internal modal coupling as well as transient responses in each resonator. Analysis in reference⁴⁷ demonstrated that the dynamics of a primary resonator, like Res 1 in our work, can be altered in a significant manner by the coupling to the secondary resonator, like Res 2 in our work. Our results further demonstrate that the secondary resonator can be more significantly influenced by the amplified amplitude-dependent damping and energy localization effect, thereby exhibiting a non-uniform average damping rate throughout the entire ringdown process, and enhancement in power flow, in the deep nonlinear asymmetric initial conditions.

By applying the amplitude ratio to the established model of coupled nonlinear systems, we successfully capture the modulated nonlinearity and its associated dynamics, thereby gaining a comprehensive understanding of the mechanism. Moreover, the experimentally measured amplitude ratios align with theoretical prediction and serve as a powerful quantitative tool, enabling us to reveal the intrinsic characteristics of the coupled resonators, including structural asymmetry, which remains elusive when using conventional swept frequency methods in nonlinear configurations. Our research has demonstrated that pronounced asymmetry within the system leads to a noticeable decrease in coherence time, impacting both linear and nonlinear scenarios. Deep asymmetry induced amplitude-dependent damping is believed as the cause, as it effectively traps energy within a specific resonator, thereby limiting the energy available for transfer to its counterpart and preventing energy exchange at a consistent rate. These insights can be linked to studies of mode-localized sensors working in the nonlinear regime and in relation to the optimal resolution around the symmetric point^{36,37}.

A deep understanding of phase locking and energy exchange depending on the specifics of each mode's frequency-energy relationship under internal resonance has been reported⁴⁷ recently. That reported general model for exploring the energy exchange between modes of a single resonator near internal resonance shows that the coherent energy transfer is only in appearance within the phase-locking period. Either entering or bypassing the phase-locking period is highly dependent on the initial conditions even with internal

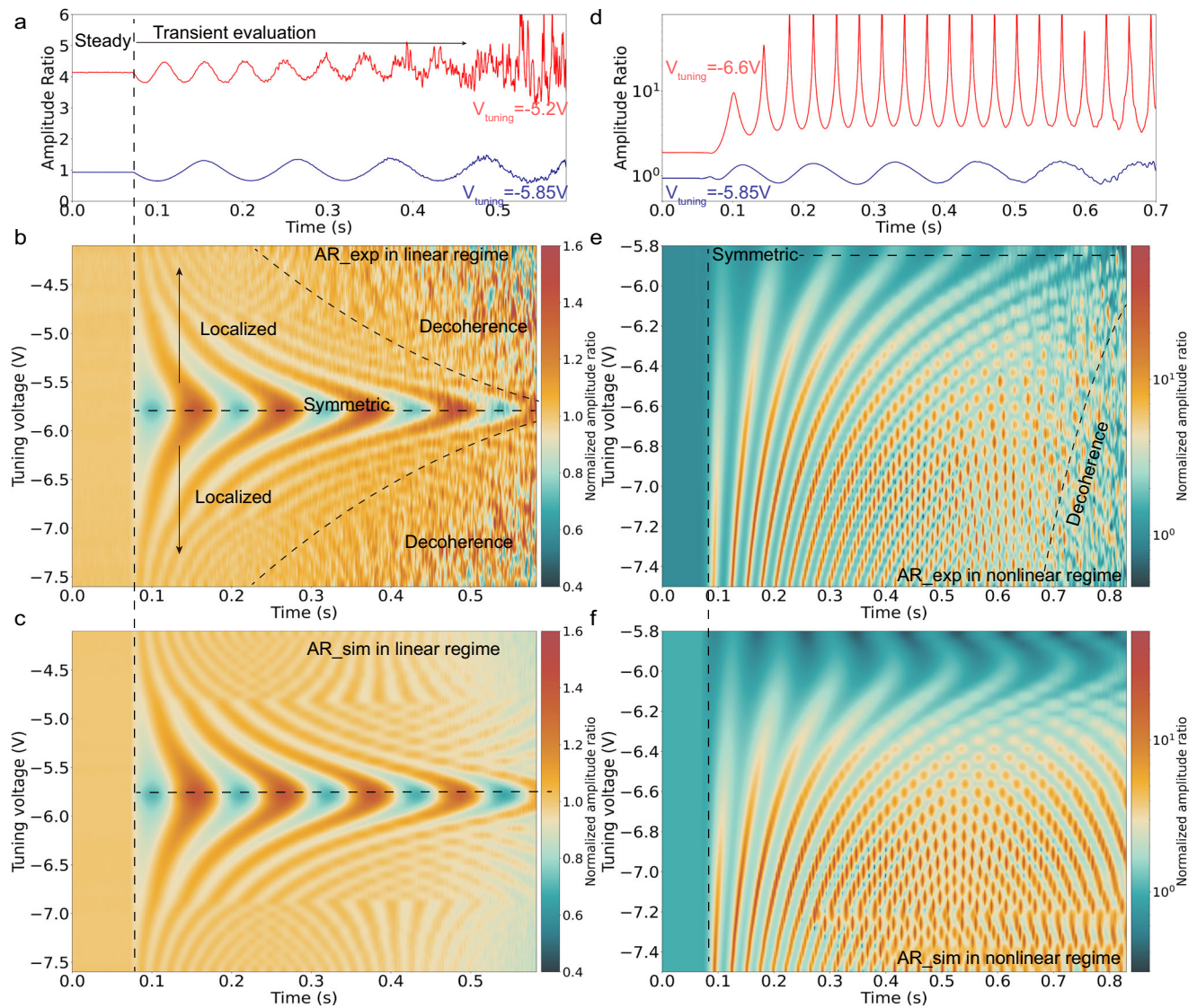


Fig. 5 | Energy transfer and redistribution portrayed using amplitude ratio. **a** Ringdown responses of the amplitude ratio with a tuning voltage of -5.85 V and -5.20 V and a drive AC level of 1 mV. **b, c** Experimentally measured and simulated amplitude ratio ringdown responses with different tuning voltages when the drive level is 1 mV. **d** Ringdown responses of the amplitude ratio with a tuning voltage of

-5.85 V and -6.60 V and a drive AC level of 30 mV. **e, f** Experimentally measured and simulated amplitude ratio ringdown responses with different tuning voltages when the drive level is 30 mV. The normalized amplitude ratio equals to 1 means that there is no transfer between resonators. Source data are provided as a Source Data file.

resonance. Other internal resonance induced energy transfer⁴⁵ bypassing phase locking has been observed with a distinctive dissipation pathway⁴¹. Our paper focuses on observing the persistent beating phenomenon and coherent energy transfer throughout the whole ringdown process until it was obscured by noise.

Using a similar multi-mode resonator as that in ref. 27, the beating-like phenomenon might be observed in the near-degenerate modes of a membrane resonator²⁹, where the near-degenerate modes exhibit different decay rates, or in a non-Hermitian system²⁴ which has two disparate modes coupled by a parametric pump. However, a crucial limitation of such system using two modes within a single resonator^{27,29} is the difficulty in independently perturbing each mode, so that the complex influence of the structural asymmetry induced energy localization nonlinearity can be simultaneously studied.

The proposed research methodology for tracking the ringdown responses of the coupled resonators can be engineered to wide applications including sensors^{30,44}, and communication systems⁴⁸. While these findings stem from a coupled micro resonator system, they can seamlessly extend to other systems such as NEMS and even

more diminutive coupled systems, for observing slight frequency modulations due to nonlinearities which cannot be easily obtained using other methods. Further studies in this area are expected to be explored. For example, the phase and frequency transitions between modes, and the time-resolved modal energy of the coupled under specific nonlinearity and additional asymmetry has not been presented in this paper. Incorporating electrostatic coupling⁴⁹ and alternative transduction methodologies such as optical detection can provide an approach to achieve flexibly controllable coupling rates and further detailed visualization of how the coupling rate influences energy transfer between modes of the coupled resonators. Uncovering these insights into the energy transfer process in resonant systems would pave the way for further understanding the dynamics of coupled nonlinear resonant systems.

Methods

Measurement setup

The motional current of the resonators is measured by purpose-designed transimpedance amplifiers. A variable voltage is applied to

the tuning electrode integrated with resonator 2 (Res 2) to provide electrostatic stiffness perturbations so that the structural asymmetry between resonators can be manually controlled. The device under test consists of two micromechanical structurally symmetric DETF resonators fixed to the same center anchor as shown in Fig. 1a. Such a quasi-rigid physical connection generates a direct mechanical coupling between resonators. Energy transfer between Res 1 and Res 2 is conducted through the coupler. The resonators are capacitively actuated and sensed through the electrodes on either side of the DETF tines. A constant 10 V DC voltage is applied to the central anchor as bias voltage for the two resonators. Thermal noise of the two resonators includes the thermomechanical noise associated with the Brownian motion and the electronic noise attributed to the power sources for bias.

Real-time transient recording using closed-loop frequency tracking

To track the transient ringdown processes of the two resonators in real time, a frequency-tracking loop including a phase-locked-loop (PLL) module from the Zurich lock-in amplifier is implemented around Res 1 to generate self-sustained oscillation before ringdown. Transient characteristics or ringdown responses of the two resonators can be obtained when turning off the feedback control switch after running a certain time in the self-sustained closed-loop steady state. After the excitation is turned off, the amplitudes start to decay towards zero, and the frequency decays toward the intrinsic natural frequency. Fortunately, the PLL module will not immediately lose the tracking function until the amplitude of Res 1 decays to a value lower than a specific threshold $\sim 20 \mu\text{V}$. Therefore, we can track the frequencies and demodulate the amplitudes of the two resonators using the time-varying tracked frequency during the ringdown process. This provides a much easier and more precise transient tracking solution compared to the conventional method of recording the ringdown sinusoidal waves and performing Fast Fourier transform.

Data availability

The source data generated in this study have been deposited in the Figshare database under <https://doi.org/10.6084/m9.figshare.28714484>. Source data are provided with this paper.

Code availability

The related code is provided at: <https://zenodo.org/records/15162385>.

References

1. Faust, T. et al. Nonadiabatic dynamics of two strongly coupled nanomechanical resonator modes. *Phys. Rev. Lett.* **109**, 037205 (2012).
2. Pernpeintner, M., Schmidt, P., Schwiendbacher, D., Gross, R. & Huebl, H. Frequency control and coherent excitation transfer in a nanostring-resonator network. *Phys. Rev. Appl.* **10**, 034007 (2018).
3. Faust, T., Rieger, J., Seitner, M. J., Kotthaus, J. P. & Weig, E. M. Coherent control of a classical nanomechanical two-level system. *Nat. Phys.* **9**, 485 (2013).
4. Zhang, Z. et al. Coherent phonon dynamics in spatially separated graphene mechanical resonators. *Proc. Natl Acad. Sci. USA* **117**, 5582–5587 (2020).
5. Frimmer, M., Gieseler, J. & Novotny, L. Cooling mechanical oscillators by coherent control. *Phys. Rev. Lett.* **117**, 163601 (2016).
6. Bozkurt, A. et al. A quantum electromechanical interface for long-lived phonons. *Nat. Phys.* **19**, 1326–1332 (2023).
7. Lorenz, H., Kohler, S., Parafilo, A., Kiselev, M. & Ludwig, S. Visualized wave mechanics by coupled macroscopic pendula: Classical analogue to driven quantum bits. *arXiv preprint. arXiv* **2207**, 09296 (2022).
8. Weaver, M. J. et al. Coherent optomechanical state transfer between disparate mechanical resonators. *Nat. Commun.* **8**, 824 (2017).
9. Zanette, D. H. Energy exchange between coupled mechanical oscillators: linear regimes. *J. Phys. Commun.* **2**, 095015 (2018).
10. Yang, Y. et al. Nonlinearity of degenerately doped bulk-mode silicon MEMS resonators. *J. Microelectromech. Syst.* **25**, 859–869 (2016).
11. Villanueva, L. G. et al. Surpassing fundamental limits of oscillators using nonlinear resonators. *Phys. Rev. Lett.* **110**, 177208 (2013).
12. Antonio, D., Zanette, D. H. & López, D. Frequency stabilization in nonlinear micromechanical oscillators. *Nat. Commun.* **3**, 1–6 (2012).
13. Czaplowski, D. A., Strachan, S., Shoshani, O., Shaw, S. W. & López, D. Bifurcation diagram and dynamic response of a MEMS resonator with a 1:3 internal resonance. *Appl. Phys. Lett.* **114**, 254104 (2019).
14. Pierre, C. Mode localization and eigenvalue loci veering phenomena in disordered structures. *J. Sound Vib.* **126**, 485–502 (1988).
15. Zhang, H. et al. On weakly coupled resonant MEMS transducers operating in the modal overlap regime. *IEEE Trans. Ultrason. Ferroelectr. Freq. Control* **68**, 1448–1457 (2020).
16. Agrawal, D. K., Woodhouse, J. & Seshia, A. A. Observation of locked phase dynamics and enhanced frequency stability in synchronized micromechanical oscillators. *Phys. Rev. Lett.* **111**, 084101 (2013).
17. Matheny, M. H. et al. Phase synchronization of two anharmonic nanomechanical oscillators. *Phys. Rev. Lett.* **112**, 014101 (2014).
18. Ganesan, A., Do, C. & Seshia, A. Phononic frequency comb via intrinsic three-wave mixing. *Phys. Rev. Lett.* **118**, 033903 (2017).
19. Czaplowski, D. A. et al. Bifurcation generated mechanical frequency comb. *Phys. Rev. Lett.* **121**, 244302 (2018).
20. Zhao, C. et al. A review on coupled MEMS resonators for sensing applications utilizing mode localization. *Sens. Actuators A Phys.* **249**, 93–111 (2016).
21. Spletzer, M., Raman, A., Wu, A. Q., Xu, X. & Reifenberger, R. Ultra-sensitive mass sensing using mode localization in coupled microcantilevers. *Appl. Phys. Lett.* **88**, 254102 (2006).
22. Meng, F. et al. Coherent coupling of metamaterial resonators with dipole transitions of boron acceptors in Si. *Opt. Lett.* **47**, 4969–4972 (2022).
23. Okamoto, H. et al. Coherent phonon manipulation in coupled mechanical resonators. *Nat. Phys.* **9**, 480 (2013).
24. Renault, P., Yamaguchi, H. & Mahboob, I. Virtual exceptional points in an electromechanical system. *Phys. Rev. Appl.* **11**, 024007 (2019).
25. Keşkekler, A. et al. Tuning nonlinear damping in graphene nanoresonators by parametric–direct internal resonance. *Nat. Commun.* **12**, 1099 (2021).
26. Zhou, X. et al. Dynamic modulation of modal coupling in microelectromechanical gyroscopic ring resonators. *Nat. Commun.* **10**, 1–9 (2019).
27. Wang, M., Perez-Morelo, D. J., Lopez, D. & Aksyuk, V. A. Persistent nonlinear phase-locking and nonmonotonic energy dissipation in micromechanical resonators. *Phys. Rev. X* **12**, 041025 (2022).
28. Chen, C., Zanette, D. H., Czaplowski, D. A., Shaw, S. & López, D. Direct observation of coherent energy transfer in nonlinear micromechanical oscillators. *Nat. Commun.* **8**, 1–7 (2017).
29. De Jong, M. et al. Beating ringdowns of near-degenerate mechanical resonances. *Phys. Rev. Appl.* **20**, 024053 (2023).
30. Zhang, H. et al. Mode-localized accelerometer in the nonlinear Duffing regime with 75 ng bias instability and 95 ng/ $\sqrt{\text{Hz}}$ noise floor. *Microsyst. Nanoeng.* **8**, 17 (2022).
31. Gil-Santos, E., Ramos, D., Pini, V., Calleja, M. & Tamayo, J. Exponential tuning of the coupling constant of coupled microcantilevers by modifying their separation. *Appl. Phys. Lett.* **98**, 123108 (2011).
32. Miller, J. M. et al. Effective quality factor tuning mechanisms in micromechanical resonators. *Appl. Phys. Rev.* **5**, 041307 (2018).
33. Limonov, M. F., Rybin, M. V., Poddubny, A. N. & Kivshar, Y. S. Fano resonances in photonics. *Nat. Photonics* **11**, 543–554 (2017).

34. Lien, Y. H. et al. Observing coherence effects in an overdamped quantum system. *Nat. Commun.* **7**, 13933 (2016).
35. Leng, H., Szychowski, B., Daniel, M. C. & Pelton, M. Strong coupling and induced transparency at room temperature with single quantum dots and gap plasmons. *Nat. Commun.* **9**, 4012 (2018).
36. Zhang, H., Chang, H. & Yuan, W. Characterization of forced localization of disordered weakly coupled micromechanical resonators. *Microsyst. Nanoeng.* **3**, 17023 (2017).
37. Pandit, M. et al. Utilizing energy localization in weakly coupled nonlinear resonators for sensing applications. *J. Microelectromech. Syst.* **28**, 182–188 (2019).
38. Nayfeh, A. H. & Mook, D. T. *Nonlinear Oscillations*. John Wiley & Sons (2008).
39. Ma, M. et al. Mode-dependent scaling of nonlinearity and linear dynamic range in a NEMS resonator. *Appl. Phys. Lett.* **125**, 083505 (2024).
40. Imboden, M. & Pritiraj, M. Dissipation in nanoelectromechanical systems. *Phys. Rep.* **534**, 89–146 (2014).
41. Güttinger, J. et al. Energy-dependent path of dissipation in nanomechanical resonators. *Nat. Nanotechnol.* **12**, 631 (2017).
42. Frimmer, M. & Novotny, L. The classical Bloch equations. *Am. J. Phys.* **82**, 947–954 (2014).
43. Luo, G. et al. Strong indirect coupling between graphene-based mechanical resonators via a phonon cavity. *Nat. Commun.* **9**, 1–6 (2018).
44. Lyu, M. et al. Computational investigation of high-order mode localization in electrostatically coupled microbeams with distributed electrodes for high sensitivity mass sensing. *Mech. Syst. Signal Process.* **158**, 107781 (2021).
45. Asadi, K., Yu, J. & Cho, H. Nonlinear couplings and energy transfers in micro- and nano-mechanical resonators: intermodal coupling, internal resonance and synchronization. *Philos. Trans. R. Soc. A* **376**, 20170141 (2018).
46. Polunin, P. M., Yang, Y., Dykman, M. I., Kenny, T. W. & Shaw, S. W. Characterization of MEMS resonator nonlinearities using the ring-down response. *J. Microelectromech. Syst.* **25**, 297–303 (2016).
47. Shoshani, O., Dykman, M. I. & Shaw, S. W. Tuning linear and nonlinear characteristics of a resonator via nonlinear interaction with a secondary resonator. *Nonlinear Dyn.* **99**, 433–443 (2020).
48. Sounas, D. L., Soric, J. & Alù, A. Broadband passive isolators based on coupled nonlinear resonances. *Nat. Electron.* **1**, 113–119 (2018).
49. Pandit, M., Zhao, C., Sobreviela, G. & Seshia, A. Practical limits to common mode rejection in mode localized weakly coupled resonators. *IEEE Sens. J.* **20**, 6818–6825 (2020).

Acknowledgements

We acknowledge financial support from the National Key R&D Program of China No. 2023YFB3208800 (H.Z.), National Science Foundation of China No. 52435012 (H.C.) and 52475606 (H.Z.), Innovation Capability Support Program of Shaanxi (Program No. 2024RS-CXTD-7, H.C.), Fundamental Research Funds for the Central Universities (H.Z. and W.Y.) and Innovate UK (A.A.S.).

Author contributions

H.Z. and A.A.S. led the methodology and the initial drafting of the manuscript. C.Z., G.S., M. Pandit, and A.A.S. designed the devices. H.Z. led the experimental characterization and performed the theoretical and data analyses. S.K. and M. Parajuli contributed to portions of the data collection. D.C. and J.S. supported the theoretical analysis. H.L., S.K., G.T., and Z.L. assisted with data visualizations and paper writing. A.A.S., W.Y., and H.C. proposed the concept and provided the experimental and computational hardware/software resources. All authors discussed the results and contributed to editing the manuscript.

Competing interests

The authors declare no competing interests.

Additional information

Supplementary information The online version contains supplementary material available at <https://doi.org/10.1038/s41467-025-59292-2>.

Correspondence and requests for materials should be addressed to Hemin Zhang, Weizheng Yuan, Honglong Chang or Ashwin A. Seshia.

Peer review information *Nature Communications* thanks Haoshen Zhu, and the other, anonymous, reviewers for their contribution to the peer review of this work. A peer review file is available.

Reprints and permissions information is available at <http://www.nature.com/reprints>

Publisher's note Springer Nature remains neutral with regard to jurisdictional claims in published maps and institutional affiliations.

Open Access This article is licensed under a Creative Commons Attribution-NonCommercial-NoDerivatives 4.0 International License, which permits any non-commercial use, sharing, distribution and reproduction in any medium or format, as long as you give appropriate credit to the original author(s) and the source, provide a link to the Creative Commons licence, and indicate if you modified the licensed material. You do not have permission under this licence to share adapted material derived from this article or parts of it. The images or other third party material in this article are included in the article's Creative Commons licence, unless indicated otherwise in a credit line to the material. If material is not included in the article's Creative Commons licence and your intended use is not permitted by statutory regulation or exceeds the permitted use, you will need to obtain permission directly from the copyright holder. To view a copy of this licence, visit <http://creativecommons.org/licenses/by-nc-nd/4.0/>.

© The Author(s) 2025